PAPER

Check for updates

Genetic control of morphological transitions in a coacervating protein template

William C. Wixson, [ID] [a] Nada Y. Naser, [ID] [a] Aditya Sonpal, [ID] [b] Jim Pfaendtner [ID] [b] and François Baneyx [ID] *[a]

Nature routinely exploits liquid–liquid phase separation (LLPS) of proteins to control the assembly and mineralization of hybrid materials. Here, we show that fusion of the Car9 silica-binding peptide to an elastin-like polypeptide (ELP) yields temperature- and sequence-programmable soft matter templates for the synthesis of silicified architectures ranging in size from nanometers to micrometers. Specifically, we demonstrate unprecedented control over the diameter of silica nanoparticles (SiNP) in the 30–60 nm range with 4 nm precision, show that a single arginine residue (R4) in the Car9 sequence underpins the transition from micelles to proteinosomes, and find that substitutions in other basic residues modulate electrostatic repulsion and solvation to enable access to kinetically trapped species. These structures, which include interconnected micelles, small ($\sim$200 nm) and large ($>$5 μm) vesicles, are readily visualized by SEM imaging following silicification. Molecular dynamics (MD) simulations and AlphaFold predictions reveal that mutations in positively charged residues alter interfacial packing, hydration, and conformational freedom of the silica-binding segments. Overall, our results establish sequence and thermal energy as synergistic levers for morphological control across length scales using solid-binding ELPs and establish mineralization as a powerful tool to visualize the structure of dynamic soft matter assemblies.

Introduction

Living systems have evolved a stunning variety of organic–inorganic hybrid materials to thrive in the environmental niches they inhabit.[1–4] The nucleation, growth, and morphogenesis of these materials, which include the calcium carbonate shells of mollusks, the hydroxyapatite bones and teeth of vertebrates, and the silica exoskeletons of diatoms, is orchestrated both spatially and temporally by high information content biomacromolecules such as nucleic acids and proteins.[5,6] Much effort has been expended to understand and harness mineralization processes with the aim of emulating the atom economy, precision, multi-functionality and effectiveness of living systems. The biomimetic and bioinspired materials thus produced have found applications in hard tissue repair, drug delivery, electronics, and many other fields.[7–9] Nevertheless, and in spite of significant progress with organic macromolecules[10,11] and polymers,[12,13] proteins enable a monomer-level control over self-assembly and inorganic templating that is difficult to duplicate with simpler molecules,[2] and nature's level of designable functionality remains unmatched.[14–16]

An attractive feature of phase changing proteins is their ability to undergo liquid–liquid phase separation (LLPS).[17] Implicated in the origins of life,[18] LLPS is exploited by nature to modulate *in vivo* partitioning and chemical exchange,[19,20] and to produce materials that range from the adhesive filaments of mussel feet to the beaks of squids.[17,21,22] Elastin-like polypeptides (ELPs),[23] are a class of phase changing proteins that undergo reversible LLPS above a transition temperature (T_t) determined by their sequence, length, and by solution conditions such as ionic strength and pH.[24–26] The thermoresponsive behavior of these low complexity proteins (most commonly a repeat of the VPGVG pentamer) has been extensively exploited in drug delivery and tissue engineering.[27,28] However, their potential in modulating the synthesis of organic–inorganic hybrid materials remains largely untapped.[29,30] ELPs offer key advantages in this space because they combine the stimuli-responsiveness and relatively simple chemistry of certain polymers with the biocompatibility of proteins and their amenability to engineering and design.[31,32]

We previously reported on the biomimetic mineralization of highly uniform silica nanoparticles (SiNPs) using a fusion protein consisting of 54 repeats of the canonical VPGVG ELP pentamer (V54) fused to a dodecameric silica-binding peptide called Car9 (DSARGFKKPGKR).[33,34] While V54 alone undergoes LLPS (*a.k.a.* coacervation) above a T_t of 40 °C,[35] fusing a cationic Car9 extension to its C-terminus causes the resulting protein

[a] *Department of Chemical Engineering, University of Washington, Seattle, WA, 98195, USA. E-mail: baneyx@uw.edu, wwixson@uw.edu, nynaser@uw.edu*

[b] *Department of Chemical & Biomolecular Engineering, North Carolina State University, Raleigh, NC, USA. E-mail: asonpal@ncsu.edu, pfaendtner@ncsu.edu*

(V54-Car9) to reversibly form micelles when the temperature is raised above 45 °C. These micelles, which consist of a coacervated ELP core surrounded by a Car9 corona and have a hydrodynamic diameter (D_h) of 31 ± 8 nm, template the silicification of 62 ± 10 nm SiNPs. Remarkably, the particles thus produced exhibit a net positive charge due to basic side-chains protruding from the silica surface and can be used to electrostatically co-assemble negatively charged nanoparticles in a variety of architectures.[34]

Here, we construct a panel of V54-Car9 variants and integrate experiments and molecular dynamics (MD) simulations to explore the influence of temperature and silica-binding segment sequence on the micellization-mineralization nexus. We show that silicification offers a powerful means to probe the structure of the underlying soft matter template and that raising the temperature and/or introducing mutations in Car9 structural residues allows for precise control of SiNP size in the 30–60 nm range with a 4 nm step size. We further show that substitutions in select Car9 basic residues enable access to a range of reversibly formed and kinetically trapped architectures that range from interconnected micelles to small (200 nm) and large (5–10 μm) vesicles. Strikingly, a single residue (R4) is responsible for the transition from micelles to vesicles which is underpinned by increased segregation of the silica-binding segment from the coacervating ELP milieu. These observations establish ELPs as a versatile system for biologically-inspired molecular assembly that offers access to much of the range of solution-state block copolymer outcomes in a single class of protein.

Experimental

DNA manipulations and protein purification

Plasmid pET24a(+)-V54-Car9, a pET24a(+) derivative encoding a fusion between a 54-repeat of the VPGVG sequence and the Car9 silica-binding peptide[33] (V54-Car9) was described previously.[34] To introduce the K8AK11A, R4QR12Q, and K7QK8QK11QR12Q (4Q) substitutions in the Car9 segment, the gene coding for V54 was excised by NdeI-HindIII digestion of pET24a(+)-V54-A3, a plasmid encoding a fusion between V54 and the A3 silver/gold-binding peptide. The cassette was ligated into the same sites of pET24a(+)-sfGFP-Car9 mutants encoding the relevant substitutions in their Car9 domains.[36,37] The R4Q and R12Q single mutants were obtained by site-directed mutagenesis of pET24a(+)-V54-Car9(R4QR12Q) using the Q5 Site-Directed Mutagenesis kit (New England Biolabs) with forward and reverse primers 5′-GCCTGGGAAGCGCTAATAACTCGAG-3′ and 5′-TTTTTAAACC CCTGAGC-3′ for the R4Q mutant, and 5′-TGACAGTGCTCGCGG GTTTAAAAAGCCTGGG-3′ and 5′-GAGCCGCCGCCAAGC-3′ for the R12Q mutant. All constructs were introduced into *E. coli* Top10 and verified by sequencing. Plasmids were next introduced into BL21(DE3) cells and proteins were expressed and purified as described.[34] Protein purity was >95%, as judged by videodensitometry of Coomassie Blue-stained SDS-PAGE gels (Fig. S1).

Silica mineralization

Silica mineralization reactions were conducted as described[34,38] except that protein solutions were pre-incubated for 10 min in a water bath held at the specified temperature prior to addition of silicic acid. The reaction was allowed to proceed for 2 h at the same temperature.

Analytical techniques

Phase transitions were monitored by UV-visible (UV-vis) spectroscopy and dynamic light scattering (DLS). For UV-vis spectroscopy, the A_{350} of protein solutions was measured as a function of temperature on a Cary 3500 spectrophotometer equipped with a Peltier temperature controller (Agilent Technologies) using a ramp rate of 1 °C per min. Protein solutions (700 μL at a concentration of 75 μM) were blanked against DI water in semi-micro quartz cuvettes. Hydrodynamic diameters and zeta (ζ) potentials were measured on a Zetasizer Nano ZS (Malvern) after 4 min of equilibration at the indicated temperatures. All variants used in this study exhibited reversible lower critical solution temperature behavior. DLS was also used to measure the D_h and ζ-potential of mineralization products after a 10-fold dilution in DI H_2O.

For scanning electron microscopy (SEM), samples were diluted 100-fold in DI H_2O, and aliquots (5 μL) were deposited on silicon wafers that were allowed to air dry overnight. Images were acquired on an Apreo-S SEM (Thermo Scientific) operated at 2 kV and 13 pA. Fluorescence spectroscopy and microscopy data were gathered after adding 2 μL of Nile red stock (10 mM in DMSO) to 1 mL of a 75 μM protein solution at room temperature. Samples were heated in a water bath at the indicated temperatures. For UV-vis spectroscopy, samples were loaded into a 96-well plate and measured with a Synergy LX Multi-Mode plate reader (BioTek). Microscopy images were collected with a Nikon Eclipse fluorescence microscope and analyzed with ImageJ.

TEM images were collected on a FEI Tecnai G2 F20 Super-Twin microscope operated at 200 keV. Cryo-TEM samples were prepared using a Vitrobot Mark IV system, with liquid ethane as the coolant. Samples were incubated on a hot plate at 65 °C and drop-cast onto C-flat holey carbon grids that were immediately plunged into liquid ethane. Imaging was performed using a Gatan CT3500 single-tilt liquid-nitrogen cryo-transfer holder.

SAXS data were collected using a Xenocs Xeuss 3.0, using Cu-Kα beam (0.15406 nm wavelength) with a Detectris Eiger 2 1M X-ray detector positioned at 1.8, 0.9, and 0.37 m from the sample. Protein solutions (200 μM) were loaded into 1.5 mm diameter quartz capillary tubes (Charles Supper), sealed with epoxy, and placed in a Peltier-type temperature-controlled stage. 2D images at each detector distance for each temperature were azimuthally averaged, merged, and reduced using XSACT 2.10 (Xenocs).

Molecular Dynamics simulations

A 5 nm × 5 nm × 12 nm simulation box was populated with nine chains consisting of five VPGVG pentapeptides (V5) fused to Car9 or one of its variants through a KLGGGS linker. Proteins

were arranged in a 3×3 grid to account for hydration and chain–chain interactions (Fig. S2). The proteins were generated using the tleap package (AMBERTools)[39] with an acetylated N-terminus, methylated C-terminus, and residues with standard charges at pH 7. Chains were aligned in visual molecular dynamics (VMD)[40] and PACKMOL[41] was used to position them in a simulation box. Systems were solvated and neutralized with Cl^{-} counterions with no excess ions. All simulations used the AMBER99SB force field in GROMACS.[42,43] Triplicate trials were conducted for each system. Trajectories were analyzed using GROMACS tools, VMD, and custom Python scripts. Further simulation details are provided in the SI.

AlphaFold predictions

Structure predictions were generated using the AlphaFold Server webtool and AlphaFold 3.0.[44] Owing to input token limits, inputs for each prediction were defined as 50 copies of truncated proteins consisting of 10 VPGVG pentapeptides (V10)

fused to Car9 or one of its variants through a KLGGGS linker. Prediction outputs were processed in Chimera.[45]

Results

Size-controlled silica nanospheres from micellar protein templates

Organisms routinely harness local changes in environmental conditions to achieve fine control over the architectures they mineralize.[46] For silica nanospheres templated by V54-Car9 micelles, the temperature was an obvious parameter to investigate. As we previously reported,[34] the V54-Car9 protein remained in a unimeric state ($D_h \sim 8$ nm) up to a temperature of 42 °C before forming transient aggregates that collapsed into micelles with a D_h of 35 nm above 45 °C (Fig. 1A). While DLS measurements did not reveal further changes in diameter as the temperature was raised to 65 °C, the size of the SiNPs silicified from the micellar templates decreased from 62 ± 10 at 45 °C,[34] to
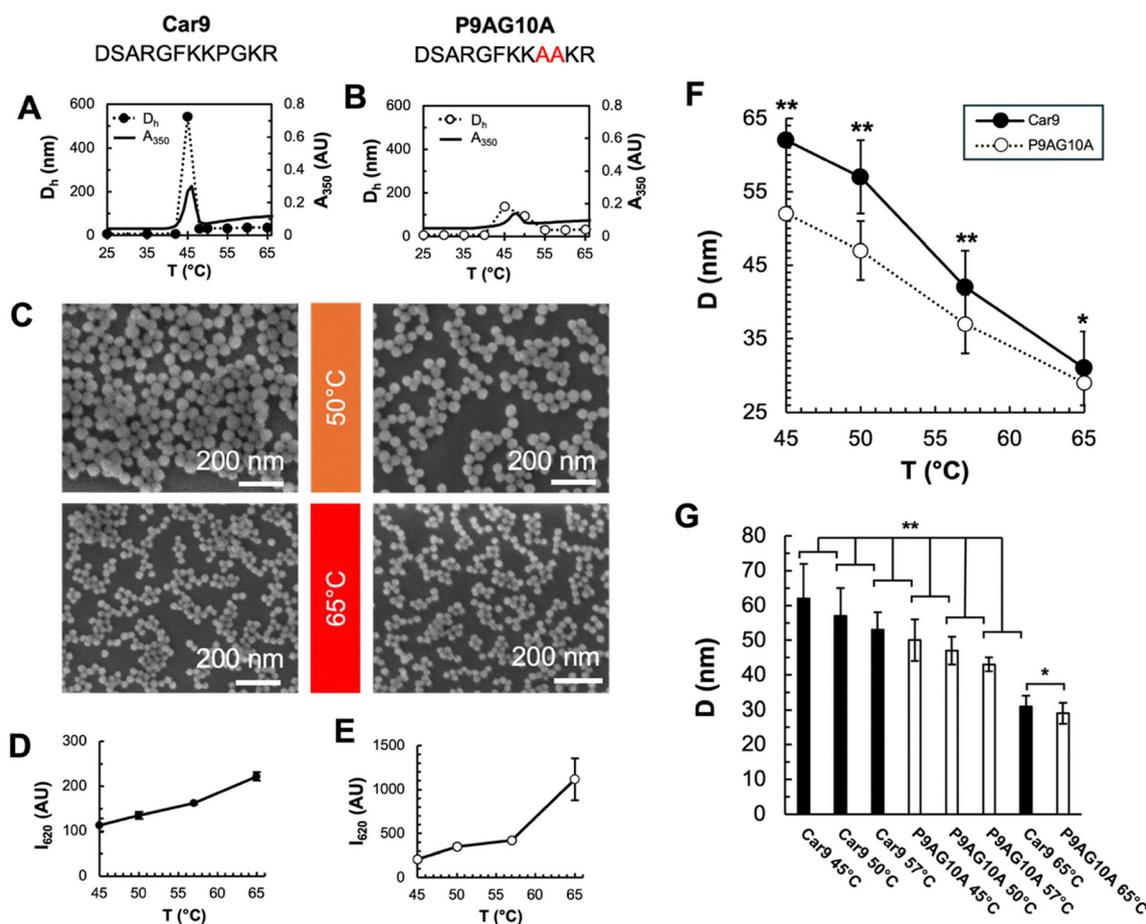

Fig. 1 Temperature and hairpin mutagenesis enable precise control over the size of protein micelles and that of the silicification products they template. (A) Turbidity data (solid line) and hydrodynamic diameters (circles) were acquired in the 25 °C to 65 °C temperature range for (A) V54-Car9 and (B) V54-P9AG10A. (C) SEM images of SiNPs templated by V54-Car9 (left) and V54-P9AG10A (right) micelles held at 50 °C or 65 °C. (D) Nile red fluorescence of V54-Car9 micelles as a function of temperature. (E) Nile red fluorescence of V54-P9AG10A micelles as a function of temperature. (F) Diameter of SiNPs templated by V54-Car9 (closed circles) and V54-P9AG10A (open circles). (G) Precise control over SiNP size between 30 and 60 nm using V54-Car9 (black bars) or V54-P9AG10A (white bars) micelles incubated at the indicated temperatures. Mean diameters and error bars were obtained by measuring 100 SiNPs on multiple micrographs. Double stars denote a $p < 0.01$ between diameters measured at the indicated temperatures. Single stars denote a $p < 0.05$.

57 ± 8 nm at 50 °C and 31 ± 3 nm at 65 °C (Fig. 1A, C and F). Based on the observation that micelles formed by diblocks of long hydrophobic and hydrophilic ELP segments undergo dehydration as the temperature is raised above T_t,[47,48] we suspected that densification of the micellar template caused by progressive desolvation of the coacervated V54 core might be responsible for the observed decrease in SiNP size. To test the idea, we probed the relative hydrophobicity of V54-Car9 micelles between 45 to 65 °C using the solvatochromic dye Nile red.[49] Fig. 1D shows that the fluorescent emission of the dye nearly doubled over this temperature range, reflecting a decrease in the water content of the core. Considering that the D_h of V54-Car9 micelles remains constant above 45 °C and that Car9 behaves as a random coil at silica surfaces,[36] the silicification of smaller SiNPs as the temperature increases is consistent with a rigidification of the Car9 corona due to progressive desolvation of the V54 core.

To bring additional support to this hypothesis, we took advantage of the fact that introduction of the P9A and G10A substitutions in the Car9 sequence disrupt a hairpin and causes the peptide to adopt a folded conformation at the silica interface in MD simulations.[36] We reasoned that a V54 fusion protein bearing these mutations (termed V54-P9AG10A) would form more compact micelles with a less mobile corona that would in turn template the mineralization of smaller SiNPs. DLS and UV-vis measurements confirmed that V54-P9AG10A formed micelles above a T_t of 50 °C and that these micelles were smaller than those produced by V54-Car9 at the same temperature (D_h = 30 nm *vs.* 35 nm; Fig. 1B). Also as predicted, the SiNPs templated by V54-P9AG10A were smaller than those produced with the wild type (D = 47 $\pm$ 4 nm *vs.* 57 $\pm$ 8 nm at 50 °C), and there was a progressive reduction in particle size as the temperature was raised to 65 °C (Fig. 1B). Finally, and consistent with a higher degree of desolvation the Nile red fluorescence of V54-P9AG10A micelles was twice that of wild type at 45 °C, and fluorescence intensity quintupled as 65 °C, denoting a significant increase in core hydrophobicity (Fig. 1E). A side-by-side comparison of the size of SiNPs templated by V54-Car9 and V54-P9AG10A micelles as a function of temperature (Fig. 1G) showed that although the largest changes in particle diameter occur below 57 °C, the dimensions of the SiNPs templated by V54-Car9 and V54-P9AG10A remains statistically different up to 65 °C.

To summarize, tuning the size of the micellar template through temperature or structural mutagenesis of the Car9 segment allows for precise control of SiNP diameter in the 30 to 60 nm range with a step size of about 4 nm (Fig. 1E). Furthermore, and unlike traditional silica, these particles carry a net positive surface charge (Table S1) that enable their use in unconventional applications such as electrostatic co-assembly.[34,50,51]

Substitutions in basic residues have distinct effects on template morphology and silicification outcomes

In block copolymer chemistry, the relative hydrophobicity of each block dictates the final structure of the assembly, and small changes in block chemistry can have a significant impact on equilibrium morphology.[52] A distinctive characteristic of the Car9 dodecapetide is a cationic character, leading us to postulate that one or more of its five positively-charged residues was implicated in V54-Car9 micellization. As an initial test of this hypothesis, and building on an extensive understanding of their influence on Car9's silica-binding behavior,[37] we introduced the K8AK11A and R4QR12Q substitutions in V54-Car9. While two basic residues are replaced by hydrophobic ones in each variant, the two proteins responded to an increase in temperature in very distinct ways.

The V54-K8AK11A lysine substitution mutant behaved largely like the wild type and the P9AG10A variant, although it underwent two transitions (at about 45 °C and 55 °C) rather than a single one at 45 °C (Fig. 2A). The first transition gave rise to micelles with a D_h of 54 $\pm$ 2 nm at 50 °C that templated the mineralization of more polydisperse SiNPs (D = 53 $\pm$ 16 nm; Fig. 2B). This size falls between that of SiNPs synthesized from V54-Car9 and V54-P9AG10A templates at the same temperature (Fig. 1D). Consistent with the elimination of two positively charged sidechains, the ζ-potential of V54-K8AK11A-templated particles was 11 $\pm$ 1 mV, about half that of SiNPs produced from V54-Car9 micelles (Table S1). Incubation above the second transition (65 °C) produced protein assemblies that were 196 $\pm$ 6 nm in D_h – larger than the 35 nm micelles produced by V54-Car9, but smaller than typical 625 $\pm$ 25 nm V54 coacervates[34] or the 602 $\pm$ 20 nm coacervates produced from V54-4Q, a variant containing glutamine mutations in four of its basic residues (K7QK8QK11QR12Q; Fig. S3A). The intermediate assemblies produced by V54-K8AK11A proved difficult to characterize by small angle X-ray scattering or cryo-electron microscopy (Fig. S4). However, we were able to exploit silicification to infer the morphology of the underlying soft template using SEM. As shown in Fig. 2B, mineralization products consisted of a network of primary particles approximately 40 nm in diameter that often interconnected with one another to form elongated chains spanning up to 20 micelle diameters. Such structures are consistent with an underlying template consisting of a percolated network of interconnected micelles.

V54-R4QR12Q behaved very differently from V54-K8AK11A with turbidity and D_h increasing with the temperature in a manner that was reminiscent of the coacervation of V54 and V54-Q4, albeit with lower final turbidity (compare Fig. 2A and Fig. S3A). However, unlike V54 or V54-Q4 (Fig. S3), V54-R4QR12Q successfully templated silica mineralization, allowing us to visualize the protein structures formed upon high temperature incubation. Silicification at 50 °C and 65 °C revealed a broad range of particle morphologies with characteristic length scales spanning 4 orders of magnitude (Fig. 2B and Fig. S6). These included interconnected 74 $\pm$ 33 nm (n = 100) particles similar to those templated by the K8AK11A variant at 65 °C (Fig. 2B, yellow arrows; Fig. S6A), nanospheres approximately 150–200 nm in diameter (orange arrows) that often merged into one another to form raspberry-like particles (red arrows), and hollow spheres that reached several micrometers in diameter. Nile Red staining and confocal microscopy confirmed that the large spheres were templated by micrometer-size vesicles that were morphologically distinct from the V54-KA8K11A micellar
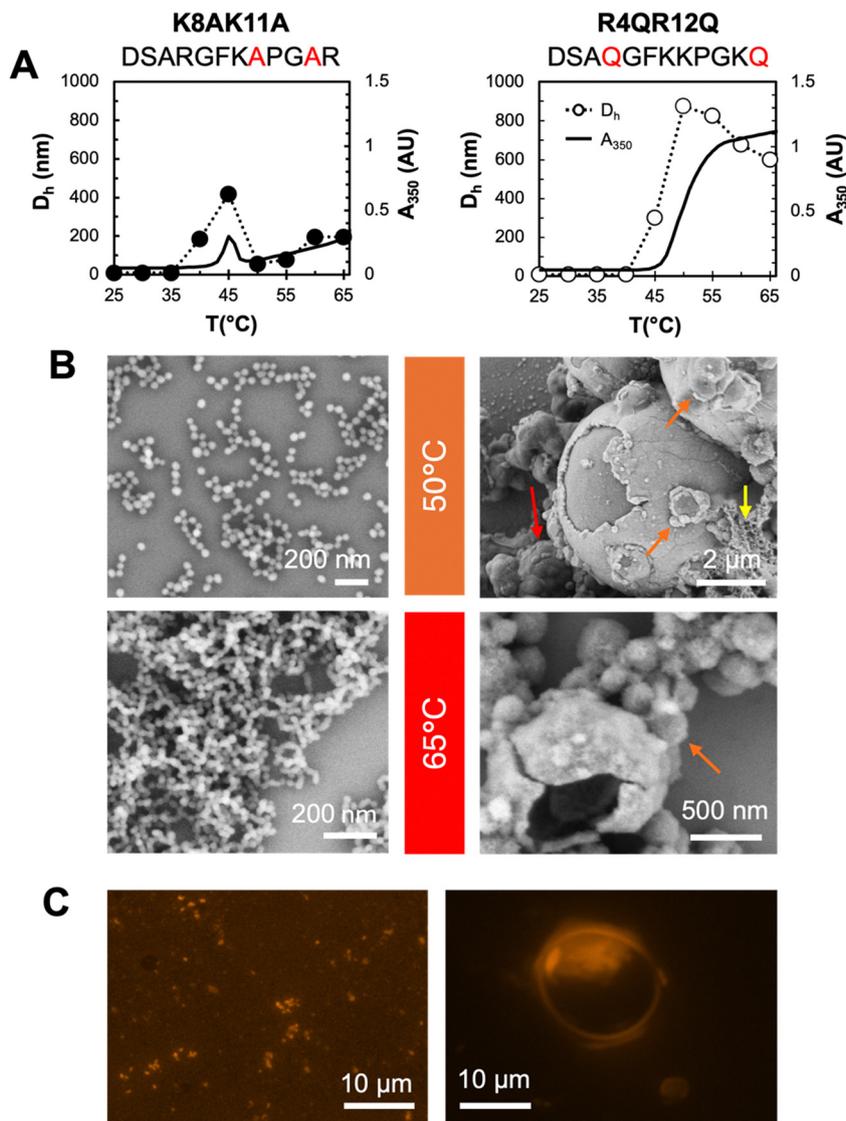
Fig. 2 Temperature dependent self-assembly and silicification products obtained from V54-K8AK11A (left) and V54-R4QR12Q (right) templates. (A) Turbidity data (solid line) and hydrodynamic diameters (circles) were acquired in the 25 °C to 65 °C temperature range. (B) SEM images of silicification products synthesized at 50 °C and 65 °C. Yellow, orange and red arrows identify interconnected SiNPs, ∼200 nm nanospheres, and raspberry-like particles, respectively. (C) Fluorescent microscopy images of Nile red-stained protein assemblies. Images for V54-K8AK11A (left) and V54-R4QR12Q (right) were acquired at 65 °C and 50 °C, respectively.

assemblies supporting the mineralization of interconnected SiNP networks (Fig. 2C).

The fact that V54-R4QR12Q templates such a broad range of mineralization products coupled with a lack of influence of a further increase in temperature suggests that the two arginine substitutions abolish the ability of V54-Car9 intermediate aggregates to collapse into stable micelles and that the protein samples a broad range of assembly states above 45 °C.

To determine if both the R4Q and R12Q mutations were required to impart this behavior, we constructed V54-R4Q and V54-R12Q single mutants and characterized their response to temperature as above. Fig. 3A shows that the R12Q mutant largely mirrored the K8AK11A variant, while V54-R4Q resembled V54-R4QR12Q, with a single transition to intermediate size species

above 45 °C. Silicification experiments confirmed that V54-R12Q templated the production of primary particles networks reminiscent of those synthesized with V54-K8AK11A at 65 °C, while V54-R4Q yielded a wide range of particle morphologies across length scales (Fig. 3B). To summarize, while the elimination of positively charged sidechains can induce micelles to fuse with one another, especially as the temperature is raised, R4 plays a unique and critical role in micelle formation.

Dissecting the role of basic residues with molecular dynamics simulations

We used all-atom molecular dynamics (MD) to gain insights on the role of basic residues in aggregation dynamics. To reduce the computational cost, we shortened the ELP segment to five
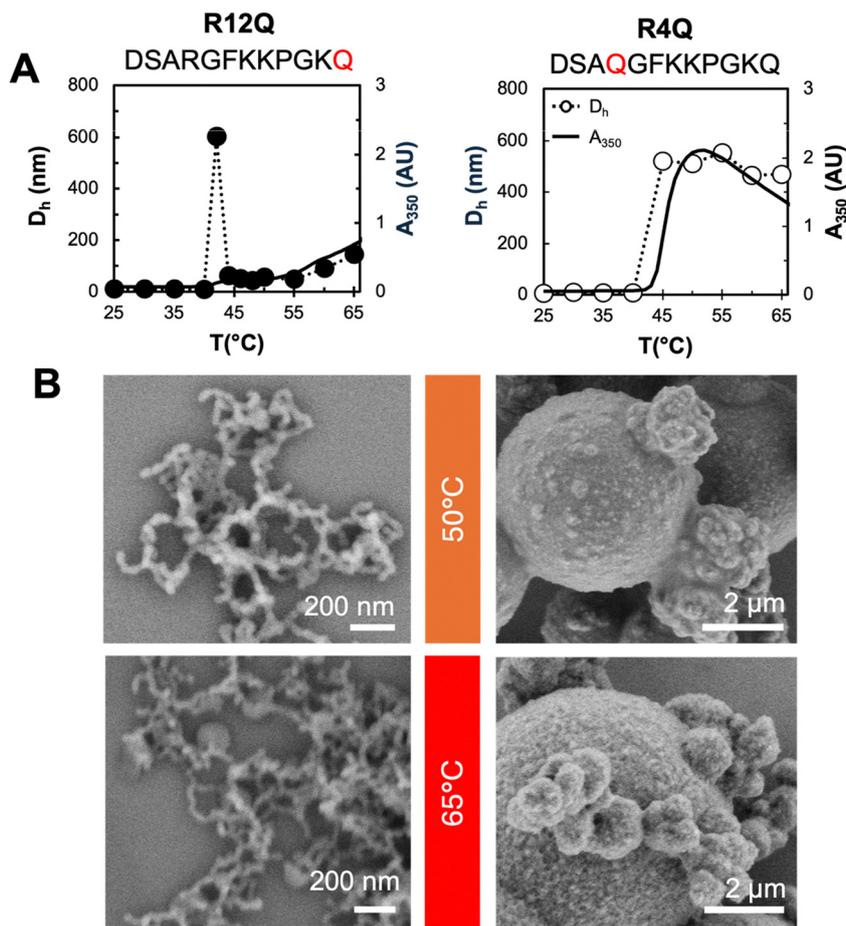
Fig. 3 Temperature dependent self assembly and silicification products for V54-R12Q (left) and V54-R4Q (right). (A) Turbidity and hydrodynamic diameter profiles for heating from 25 °C to 65 °C. (B) SEM images of silicification products synthesized at 50 and 65 °C.

VPGVG repeats (V5), connected them to Car9 or one of its mutants through a KLGGGS linker, and constructed a polymer brush-like system to represent a section of the micelle core (Fig. S2). Nine chains were placed in the simulation box, allowed to equilibrate, and the density of Car9/Car9 variant atoms was quantified along the z-axis of the simulation box (Fig. 4, blue traces), and compared to the z-coordinate of the V5-linker block's center of mass (COM, dashed lines). The exercise revealed the interface between silica-binding segments (orange) and V5-linker segments (black and gray, respectively). For systems mimicking micelle-forming proteins (*i.e.*, V5-Car9 and V5-P9AG10A), the silica-binding segments exhibited a broad distribution of densities along the z-axis and overlapped with the V5-linker COM (Fig. 4A and B). This is consistent with routine excursions of silica-binding domains in the ELP-linker milieu. By contrast, systems based on proteins that template micrometer-scale spherical structures (V5-R4QR12Q and V5-R4Q) exhibited a single narrow peak and spatial resolution between silica-binding segments and ELP-linker segments (Fig. 4C and D). Finally, systems based on proteins templating SiNP networks (V5-K8AK11A and V5-R12Q) displayed an intermediate behavior (Fig. 4E and F). Importantly, these results were consistently observed across triplicate trials.

To understand the energetic basis of these differences, we performed an analysis of interchain and chain-water Lennard Jones (LJ) and Coulombic interactions (Fig. S10). Consistent with their similar temperature responses and silica templating activities, V5-Car9 and V5-P9AG10A had comparable energy profiles. By contrast, V5-R4QR12Q and V5-R4Q exhibited stronger chain–chain interactions and weaker interactions with water relative to V5-Car9. This implies an enhanced propensity for self-association that is fully consistent with the segregation of ELP-linker segments observed in Fig. 4C and D. The energetic response of the V5-K8K11A and V5-R12Q systems was less easy to interpret with V5-R12Q behaving much like V5-R4QR12Q and V5-R4Q, and V5-K8AK11A demonstrating an even higher tendency towards hydration compared to V5-Car9. For these two variants, energetic mapping might fall short of predicting self-assembly behavior.

AlphaFold 3.0 as a rapid tool for predicting the influence of basic residues substitutions on ELP-mediated assembly

AlphaFold 3.0 is a diffusion-based model that enables high accuracy modeling of the structure of complexes comprising proteins, nucleic acids, small molecules, ions and modified residues.[44] Building upon AlphaFold-Multimer (v. 2.3), the 3.0 version uses
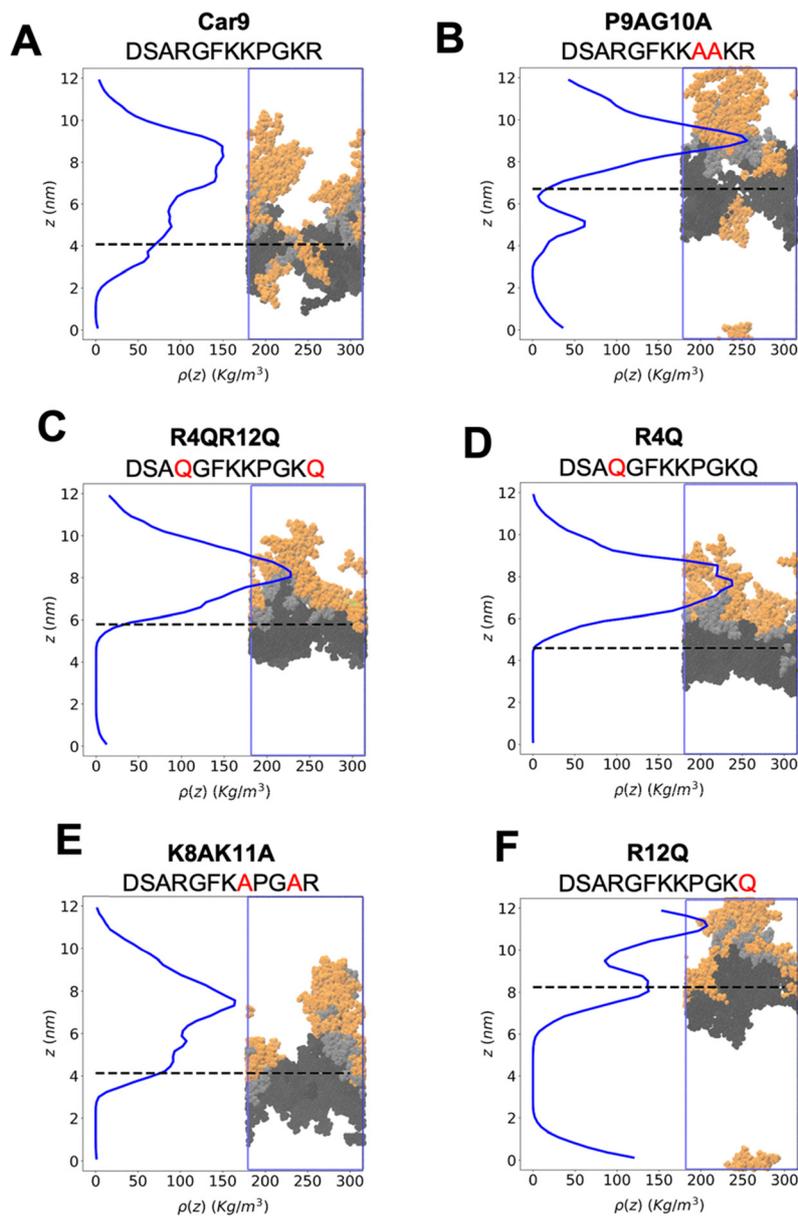
Fig. 4 Density profiles and end of simulation poses of nine copies of V5 repeats fused to: (A) Car9, (B) P9AG10A, (C) R4QR12Q, (D) R4Q, (E) K8AK11A, and (F) R12Q. Left panels show the density profiles of all atoms in the silica-binding segments of the indicated variants along the z-axis of the simulation box (solid blue line). The COM of all atoms in the ELP segments is represented by a black dashed line. Right panels show corresponding poses at the end of the simulation with silica-binding segments colored orange, ELP segments colored dark gray, and linkers colored light gray.

cross-distillation to enhance training data and improve predictive power for protein–protein interactions and disordered regions. We used AlphaFold 3.0 to compare the predicted interactions of 50 copies of the variants under study to the structures experimentally revealed by silicification. Owing to input token restrictions, each protein was modeled as 10 repeats of the VPGVG sequence (V10) connected to Car9 or its variants *via* a KLGGGS linker. The ability of AlphaFold 3.0 to predict the structure of intrinsically disordered proteins or interactions between proteins with repetitive sequences is inherently low.[53] We were therefore not surprised that predicted template modelling scores (pTM) and interface predicted modelling scores (ipTM) fell in the range of 0.26 to 0.31 (out of 1).

However, there were clear differences between the structures offered by the model. As shown in Fig. 5A, the 50 copies of V10-Car9 formed a micelle-like arrangement consisting of a dense ELP core surrounded by a corona of rather evenly distributed surface Car9 clusters. By contrast, the ELP segments of V10-R4QR12Q chains adopted a ring-like structure belted by well-ordered silica-binding segments (Fig. 5B). In fact, all assembled architectures predicted by AlphaFold were consistent with those revealed by silicification: V10-Car9 and V10-P9AG10A collapsed into micelle-like structures with a dense core while V10-K8AK11A, V10-R12Q, V10-R4QR12Q and V10-R4Q adopted a "belted barrel" conformation. The progressive ordering of silica-binding segments was
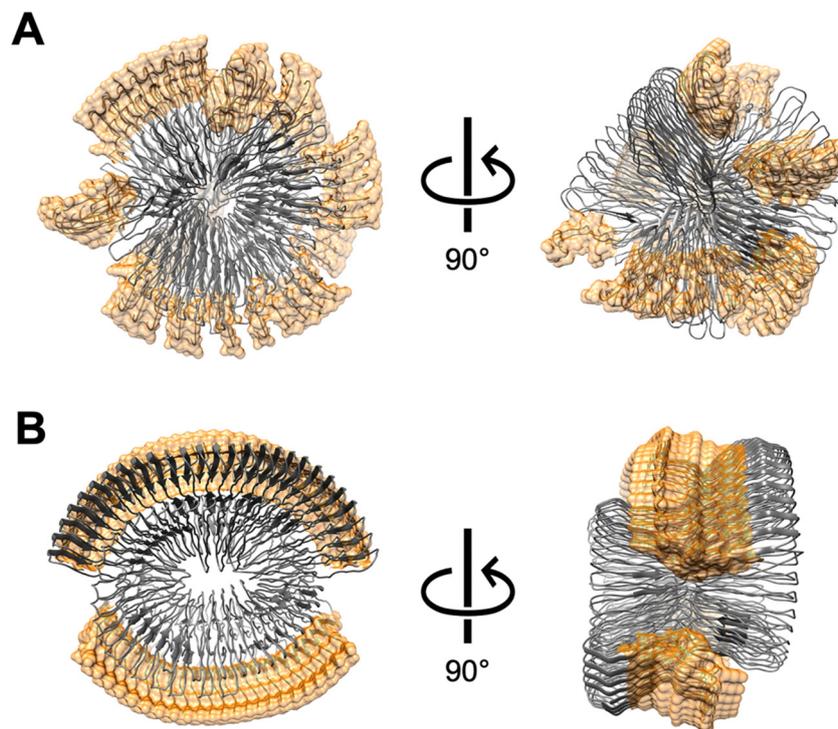
Fig. 5 AlphaFold predictions of assembled structures obtained with 50 copies of (A) V10-Car9 or (B) V10-R4QR12Q. The silica-binding segments are colored orange.

consistent with the evolution of the latter variants into interconnected micelles, small vesicles and ultimately proteinosomes (Fig. S11). While these results indicate that AlphaFold holds promise for predicting structural outcomes in the assembly of multiple copies of intrinsically disordered proteins, additional work will be needed to validate the approach.

Discussion

We have described a panel of proteins composed of an ELP segment fused to a silica-binding peptide that assemble into block copolymer-like architectures upon temperature-induced coacervation of their ELP domains. All variants are based on the V54-Car9 framework, a protein that undergoes micellization above 45 °C.[34] Remarkably, the introduction of one or two mutations in the hydrophilic Car9 dodecamer of the 286 residues-long fusion protein is sufficient to produce structures ranging from isolated micelles and interconnected micellar networks to vesicular proteinosomes that can reach tens of micrometers. While the existence and morphological evolution of such diverse soft matter structures would normally be challenging to document, silicification enabled their facile visualization by SEM.

On the precision end of the spectrum, our ability to finely control the diameter of SiNPs between 30 and 60 nm in 4 nm steps far exceeds the performance of Stöber synthesis and other block copolymer templating methods in this size range.[54–56] Precision is achieved by decreasing the size of the micellar template through temperature control of ELP core desolvation

and/or by reducing the mobility of the solid-binding segment by mutagenesis of structurally significant residues (*i.e.*, the P9G10A hairpin). Such size control is important for designing SiNP systems with specified optical and electromagnetic properties as well as for controlling strength and toughness in composite materials.[57]

While conversion of micelles to large vesicles is ultimately mediated by a single arginine residue (R4), a continuum of conformations that are in dynamic equilibrium with each other can be accessed by substituting other basic residues for neutral ones in the Car9 segment, and by increasing the temperature. For instance, interconnected micelles that template the mineralization of porous silica networks are formed when the V54-K8AK11A variant is incubated at 65 °C or when the V54-R4Q is heated to 50 °C. However, ~200 nm silicified vesicles begin to appear when V54-R12Q is incubated at 65 °C (Fig. 3B) or V54-K8AK11A is incubated at 75 °C (Fig. S9). In other words, the introduction of mutations that reduce electrostatic repulsion and the input of thermal energy can be exploited individually and synergistically to dislodge structures from kinetically trapped states and control the formation of the architectures that are schematically illustrated in Fig. 6. This is significant because previous success in converting spherical micelles to interconnected micelles has necessitated rather drastic changes in surfactant or polymer chemistry such as modification of block length ratios or wholesale change in composition.[58] We also note that whereas vesicles have been thermally accessed using other ELP fusion proteins,[59–61] the fusion partner has always been a globular protein rather than a 12 amino acid peptide.
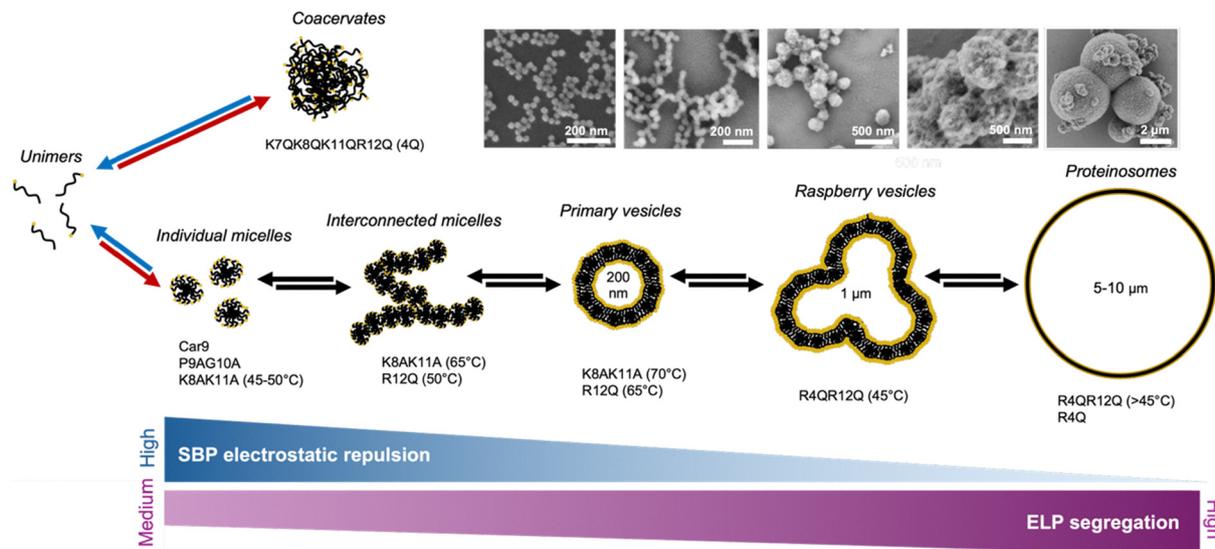
Fig. 6 Assembly pathways of V54-Car9 variants. While 4Q mutants containing glutamine substitutions in 4 of their 5 basic Car9 residues form standard coacervates (top), the wild type protein assembles into individual micelles above 45 °C (bottom). Other variants access a continuum of nonequilibrium structures depending on the identity of the substitutions and the incubation temperature. Mutants capable of accessing the large vesicle state (R4Q and R4QR12Q) are in dynamic equilibrium with other morphologies (raspberry vesicles, primary vesicles, interconnected micelles and individual micelles). Progression from micelles to vesicles is associated with decrease interchain electrostatic repulsion and increased segregation of ELP and silica-binding segments within each chain.

In surfactant and block copolymer literature, the transition from micelles to vesicles is captured by the packing parameter p,

$$p = \frac{v}{a_0 l_c}$$

where v is the volume of the cone occupied by a chain, a_0 is the surface area occupied by the head group, and l_c is the contour length of the chain. Micelles dominate when $p \leq \frac{1}{3}$ while vesicles do when $p \geq \frac{1}{2}$. Wormlike micelles occupy the space between these cutoff values.[62] The contour length of the proteins used in our study is the same. However, a_0 depends on the extent of electrostatic repulsion between head groups (in our case the silica-binding segments) and this parameter likely underpins the morphological differences we observe when variants are assembled at a prescribed temperature.

An analysis of the Coulombic and Lennard-Jones (LJ) energetics from MD simulations provides support for this idea (Fig. S10). As expected from their common micellization behavior, surrogates for V54-Car9 and the P9AG10A variant exhibit similar chain–chain interaction energetics. This implies nearly identical a_0 and therefore p values. (The slight increase in chain-water LJ repulsion energy for the P9AG10A variant is consistent with a higher degree of core desolvation.) By contrast, surrogates for the R4Q, R12Q and R4QR12Q variants experience weaker chain–chain Coulombic repulsion relative to the wild type. This should lower a_0 and favor vesicle formation, as is observed experimentally. Furthermore, a clustering analysis of MD trajectories (Fig. S13) indicates that surrogates for variants that form interconnected micelle (V54-K8AK11A and V54-R12Q) have lower conformational freedom relative to the R4QR12Q and R4Q vesicle-forming variants (Fig. S14A and Table S2). This is consistent with the observation that rigid copolymer chains prefer to form elongated micellar structures by aligning hydrophobic blocks parallel to one another to reduce water contact.[63]

Where thermal energy is concerned, the temperature-dependent entropic forces driving the desolvation of ELP segments are finely balanced against the electrostatic repulsion of silica-binding "head groups" such that an increase in temperature can also shift the balance between micellization (high electrostatic repulsion, moderate desolvation and segregation of Car9 and ELP segments) and vesicle formation (low electrostatic repulsion, high desolvation and segment segregation) in the dynamic equilibrium of canonical structures depicted in Fig. 6.

Beyond ensemble electrostatic and desolvation considerations, our results show that the amino acid sequence of the silica-binding segment – and by implication the spectrum of conformations it enables each chain to access – is critical in determining both assembly outcomes and the details of the assembly. The former point is best illustrated by the fact that although the V54-R4Q and V54-R12Q variants both lack one arginine residue, they form very different architectures at high temperatures (Fig. 3). Analysis of MD trajectories uncovered more subtle effects, such as the more compact nature of the silica-binding segment in V54-Car9 and its P9AG10A variant, and the higher structural diversity that this segment experiences in the wild type relative to V54-P9AG10A, which likely influences micelle desolvation efficiency.

Conclusions

In nature, small changes in the amino acid sequence of a protein – often in a single residue – can have a profound impact

on self-assembly and mineralization outcomes. The conse-quences may be deleterious, as exemplified by the formation of toxic oligomers in neurodegenerative diseases[64] and defec-tive tooth enamel in amelogenesis imperfecta.[65] Yet, mutations often confer gain of function by increasing fitness and adapt-ability to diverse environments,[66] and as such, are a key driver of evolution.[67,68]

Here, we have shown that one or two substitutions in a 12 residues-long silica-binding peptide can dramatically influence the temperature-dependent assembly behavior of the 270 residues-long ELP to which it is fused, enabling access to architectures spanning four orders of magnitude in characteristic lengths. The underlying morphologies were revealed by silifica-tion of the soft matter templates followed by SEM imaging, a simple and inexpensive alternative to the cryo-TEM, x-ray and neutron scattering approaches that are typically used to charac-terize micelles and vesicles formed by surfactants and block copolymers.[69,70] Additionally, while dynamic transitions from micelles to vesicles have been observed with the latter molecules,[71,72] the process typically requires wholesale changes in sequence, composition, or the mixing of species.[73] Finally, while peptide amphiphiles have been used to assemble micelles and vesicles across scales, control is generally achieved by manipulating non-peptide components (namely, the length, number, and identity of the hydrophobic non-peptide tails), and little attention has been paid to leveraging differences in the sequence of the hydrophilic block.[74,75] By comparison, the sequence-defined simplicity of our solid-binding ELP system, its sensitivity to mutations, and its amenability to engineering are unparalleled. Finally, the ability of MD simulations and of the AlphaFold model to predict similar structural outcomes for the panel of V54-Car9 variants bodes well for the design of other solid-binding intrinsically disordered proteins that will support the synthesis of environmentally-responsive functional matter.

Author contributions

This manuscript was written through the contributions of all authors.

Conflicts of interest

The authors declare the following competing financial interest(s): F. B. declares competing financial interest in Proteios Technol-ogy, Inc. which researches and commercializes Car9-based technologies.

Data availability

The data supporting this article have been included as part of the supplementary information (SI). Supplementary informa-tion: supplementary methods, characterization data, micro-scopy images, molecular dynamics data. See DOI: https://doi.org/10.1039/d5sm01047k.

Acknowledgements

References

1 National Research Council Committee on Research Oppor-tunities in Biology, Molecular Structure and Function, *Opportunities in Biology*, National Academies Press, 1989.

2 L. Shao, J. Ma, J. L. Prelesnik, Y. Zhou, M. Nguyen, M. Zhao, S. A. Jenekhe, S. V. Kalinin, A. L. Ferguson, J. Pfaendtner, C. J. Mundy, J. J. De Yoreo, F. Baneyx and C.-L. Chen, Hierarchical Materials from High Information Content Macromolecular Building Blocks: Construction, Dynamic Interventions, and Prediction, *Chem. Rev.*, 2022, **122**(24), 17397–17478, DOI: 10.1021/acs.chemrev.2c00220.

3 J. F. Lutz, J. M. Lehn, E. W. Meijer and K. Matyjaszewski, From Precision Polymers to Complex Materials and Systems, *Nat. Rev. Mater.*, 2016, **1**(5), 1–14, DOI: 10.1038/natrevmats.2016.24.

4 M. A. R. Meier and C. Barner-Kowollik, A New Class of Materials: Sequence-Defined Macromolecules and Their Emerging Applications, *Adv. Mater.*, 2019, **31**(26), 1806027, DOI: 10.1002/adma.201806027.

5 D. Athanasiadou and K. M. M. Carneiro, DNA Nanostruc-tures as Templates for Biomineralization, *Nat. Rev. Chem.*, 2021, **5**(2), 93–108, DOI: 10.1038/s41570-020-00242-5.

6 K. Futagawa, Y. Kato and M. Suzuki, Conformational Analysis of Biomineral Proteins Interacting with Inorganic Minerals Using Dispersive Mineral Particles for Solution NMR, *CrystEng-Comm*, 2025, **27**(14), 2043–2063, DOI: 10.1039/D4CE01253D.

7 I. Yamashita, Biosupramolecules for Nano-Devices: Biominer-alization of Nanoparticles and Their Applications, *J. Mater. Chem.*, 2008, **18**(32), 3813–3820, DOI: 10.1039/B810190F.

8 S. Yao, B. Jin, Z. Liu, C. Shao, R. Zhao, X. Wang and R. Tang, Biomineralization: From Material Tactics to Biological Strategy, *Adv. Mater.*, 2017, **29**(14), 1605903, DOI: 10.1002/adma.201605903.

9 L. Ma, Y. Sun, Q. Cheng, Z. Yang, J. Wang, Z. Xu, M. Yang and Y. Shuai, Silk Protein-Mediated Biomineralization: From Bioinspired Strategies and Advanced Functions to Biomedi-cal Applications, *ACS Appl. Mater. Interfaces*, 2023, **15**(28), 33191–33206, DOI: 10.1021/acsami.3c04067.

10 S. Che, A. E. Garcia-Bennett, T. Yokoi, K. Sakamoto, H. Kunieda, O. Terasaki and T. Tatsumi, A Novel Anionic Surfactant Templating Route for Synthesizing Mesoporous

Silica with Unique Structure, *Nat. Mater.*, 2003, **2**(12), 801–805, DOI: 10.1038/nmat1022.

11 K.-W. Park, J.-Y. Kim, H.-J. Seo and O.-Y. Kwon, Preparation of Mesoporous Silica by Nonionic Surfactant Micelle–Templated Gelation of Na2SiO3 and H2SiF6 and Application as a Catalyst Carrier for the Partial Oxidation of CH4, *Sci. Rep.*, 2019, **9**(1), 13360, DOI: 10.1038/s41598-019-50053-y.

12 Y. Zou, X. Zhou, J. Ma, X. Yang and Y. Deng, Recent Advances in Amphiphilic Block Copolymer Templated Mesoporous Metal-Based Materials: Assembly Engineering and Applications, *Chem. Soc. Rev.*, 2020, **49**(4), 1173–1208, DOI: 10.1039/C9CS00334G.

13 K. Vallé, P. Belleville, F. Pereira and C. Sanchez, Hierarchically Structured Transparent Hybrid Membranes by in Situ Growth of Mesostructured Organosilica in Host Polymer, *Nat. Mater.*, 2006, **5**(2), 107–111, DOI: 10.1038/nmat1570.

14 A. E. Danks, S. R. Hall and Z. Schnepp, The Evolution of 'Sol–Gel' Chemistry as a Technique for Materials Synthesis, *Mater. Horiz.*, 2016, **3**(2), 91–112, DOI: 10.1039/C5MH00260E.

15 T. Kato, A. Sugawara and N. Hosoda, Calcium Carbonate–Organic Hybrid Materials, *Adv. Mater.*, 2002, **14**(12), 869–877, DOI: 10.1002/1521-4095.

16 J.-S. Park, Y. Sunwoo, D. Chakraborty, C. Gunathilake, Y. Du and E.-B. Cho, 3D Interconnected Polymer/Mesoporous Silica Nanoparticle Hybrid Materials with Hierarchical Macro/Meso-Structures for Heavy Metal Adsorption, *New J. Chem.*, 2024, **48**(16), 7503–7516, DOI: 10.1039/D3NJ05887E.

17 S. Boeynaems, S. Alberti, N. L. Fawzi, T. Mittag, M. Polymenidou, F. Rousseau, J. Schymkowitz, J. Shorter, B. Wolozin, L. Van Den Bosch, P. Tompa and M. Fuxreiter, Protein Phase Separation: A New Phase in Cell Biology, *Trends Cell Biol.*, 2018, **28**(6), 420–435, DOI: 10.1016/j.tcb.2018.02.004.

18 E. Spruijt, Open Questions on Liquid–Liquid Phase Separation, *Commun. Chem.*, 2023, **6**(1), 23, DOI: 10.1038/s42004-023-00823-7.

19 M. Naz, L. Zhang, C. Chen, S. Yang, H. Dou, S. Mann and J. Li, Self-Assembly of Stabilized Droplets from Liquid–Liquid Phase Separation for Higher-Order Structures and Functions, *Commun. Chem.*, 2024, **7**(1), 79, DOI: 10.1038/s42004-024-01168-5.

20 M. Novakovic, Y. Han, N. C. Kathe, Y. Ni, L. Emmanouilidis and F. H.-T. Allain, LLPS REDIFINE Allows the Biophysical Characterization of Multicomponent Condensates without Tags or Labels, *Nat. Commun.*, 2025, **16**(1), 4628, DOI: 10.1038/s41467-025-59759-2.

21 M. Sumper, A Phase Separation Model for the Nanopatterning of Diatom Biosilica, *Science*, 2002, **295**(5564), 2430–2433, DOI: 10.1126/science.1070026.

22 Y. Sun, Z. W. Lim, Q. Guo, J. Yu and A. Miserez, Liquid–Liquid Phase Separation of Proteins and Peptides Derived from Biological Materials: Discovery, Protein Engineering, and Emerging Applications, *MRS Bull.*, 2020, **45**(12), 1039–1047, DOI: 10.1557/mrs.2020.301.

23 D. W. Urry, Physical Chemistry of Biological Free Energy Transduction as Demonstrated by Elastic Protein-Based Polymers, *J. Phys. Chem. B*, 1997, **101**(51), 11007–11028, DOI: 10.1021/jp972167t.

24 Y. Zhao, M. K. Singh, K. Kremer, R. Cortes-Huerto and D. Mukherji, Why Do Elastin-Like Polypeptides Possibly Have Different Solvation Behaviors in Water–Ethanol and Water–Urea Mixtures, *Macromolecules*, 2020, **53**(6), 2101–2110, DOI: 10.1021/acs.macromol.9b02123.

25 C. P. Winlove, K. H. Parker, A. R. Ewins and N. E. Birchler, The Polyelectrolyte Properties of Elastin, *J. Biomech. Eng.*, 1992, **114**(3), 293–300, DOI: 10.1115/1.2891386.

26 J. A. MacKay, D. J. Callahan, K. N. FitzGerald and A. Chilkoti, Quantitative Model of the Phase Behavior of Recombinant pH-Responsive Elastin-Like Polypeptides, *Biomacromolecules*, 2010, **11**(11), 2873–2879, DOI: 10.1021/bm100571j.

27 J. R. McDaniel, D. J. Callahan and A. Chilkoti, Drug Delivery to Solid Tumors by Elastin-like Polypeptides, *Adv. Drug Delivery Rev.*, 2010, **62**(15), 1456–1467, DOI: 10.1016/j.addr.2010.05.004.

28 D. L. Nettles, A. Chilkoti and L. A. Setton, Applications of Elastin-like Polypeptides in Tissue Engineering, *Adv. Drug Delivery Rev.*, 2010, **62**(15), 1479–1485, DOI: 10.1016/j.addr.2010.04.002.

29 E. Wang, S.-H. Lee and S.-W. Lee, Elastin-Like Polypeptide Based Hydroxyapatite Bionanocomposites, *Biomacromolecules*, 2011, **12**(3), 672–680, DOI: 10.1021/bm101322m.

30 W. Han, S. R. MacEwan, A. Chilkoti and G. P. López, Bio-Inspired Synthesis of Hybrid Silica Nanoparticles Templated from Elastin-like Polypeptide Micelles, *Nanoscale*, 2015, **7**(28), 12038–12044, DOI: 10.1039/C5NR01407G.

31 Q. Zeng, M. S. Desai, H.-E. Jin, J. H. Lee, J. Chang and S.-W. Lee, Self-Healing Elastin–Bioglass Hydrogels, *Biomacromolecules*, 2016, **17**(8), 2619–2625, DOI: 10.1021/acs.biomac.6b00621.

32 Y. Zhou, Y. Zhou, L. Gao, C. Wu and J. Chang, Synthesis of Artificial Dental Enamel by an Elastin-like Polypeptide Assisted Biomimetic Approach, *J. Mater. Chem. B*, 2018, **6**(5), 844–853, DOI: 10.1039/C7TB02576A.

33 B. L. Coyle and F. Baneyx, A Cleavable Silica-Binding Affinity Tag for Rapid and Inexpensive Protein Purification, *Biotechnol. Bioeng.*, 2014, **111**(10), 2019–2026, DOI: 10.1002/bit.25257.

34 N. Y. Naser, W. C. Wixson, H. Larson, B. M. Cossairt, L. D. Pozzo and F. Baneyx, Biomimetic Mineralization of Positively Charged Silica Nanoparticles Templated by Thermoresponsive Protein Micelles: Applications to Electrostatic Assembly of Hierarchical and Composite Superstructures, *Soft Matter*, 2025, **21**(2), 166–178, DOI: 10.1039/D4SM00907J.

35 G. C. Yeo, B. Aghaei-Ghareh-Bolagh, E. P. Brackenreg, M. A. Hiob, P. Lee and A. S. Weiss, Fabricated Elastin, *Adv. Healthcare Mater.*, 2015, **4**(16), 2530–2556, DOI: 10.1002/adhm.201400781.

36 B. Hellner, S. Alamdari, H. Pyles, S. Zhang, A. Prakash, K. G. Sprenger, J. J. De Yoreo, D. Baker, J. Pfaendtner and F. Baneyx, Sequence–Structure–Binding Relationships Reveal Adhesion Behavior of the Car9 Solid-Binding Peptide: An Integrated Experimental and Simulation Study, *J. Am. Chem. Soc.*, 2020, **142**(5), 2355–2363, DOI: 10.1021/jacs.9b11617.

37 B. Hellner, A. E. Stegmann, K. Pushpavanam, M. J. Bailey and F. Baneyx, Phase Control of Nanocrystalline Inclusions in Bioprecipitated Titania with a Panel of Mutant Silica-

Binding Proteins, *Langmuir*, 2020, **36**(29), 8503–8510, DOI: 10.1021/acs.langmuir.0c01108.

38 N. Kröger, R. Deutzmann and M. Sumper, Polycationic Peptides from Diatom Biosilica That Direct Silica Nano-sphere Formation, *Science*, 1999, **286**(5442), 1129–1132, DOI: 10.1126/science.286.5442.1129.

39 D. A. Case, H. M. Aktulga, K. Belfon, D. S. Cerutti, G. A. Cisneros, V. W. D. Cruzeiro, N. Forouzesh, T. J. Giese, A. W. Götz, H. Gohlke, S. Izadi, K. Kasavajhala, M. C. Kaymak, E. King, T. Kurtzman, T.-S. Lee, P. Li, J. Liu, T. Luchko, R. Luo, M. Manathunga, M. R. Machado, H. M. Nguyen, K. A. O'Hearn, A. V. Onufriev, F. Pan, S. Pantano, R. Qi, A. Rahnamoun, A. Risheh, S. Schott-Verdugo, A. Shajan, J. Swails, J. Wang, H. Wei, X. Wu, Y. Wu, S. Zhang, S. Zhao, Q. Zhu, T. E. I. Cheatham, D. R. Roe, A. Roitberg, C. Simmerling, D. M. York, M. C. Nagan and K. M. Merz, AmberTools, *J. Chem. Inf. Model.*, 2023, **63**(20), 6183–6191, DOI: 10.1021/acs.jcim.3c01153.

40 W. Humphrey, A. Dalke and K. Schulten, VMD: Visual Molecular Dynamics, *J. Mol. Graphics*, 1996, **14**(1), 33–38, DOI: 10.1016/0263-7855(96)00018-5.

41 L. Martínez, R. Andrade, E. G. Birgin and J. M. Martínez, PACKMOL: A package for building initial configurations for molecular dynamics simulations, *J. Comput. Chem.*, 2009, **30**(13), 2157–2164, DOI: 10.1002/jcc.21224.

42 M. J. Abraham, T. Murtola, R. Schulz, S. Páll, J. C. Smith, B. Hess and E. Lindahl, GROMACS: High Performance Molecular Simulations through Multi-Level Parallelism from Laptops to Supercomputers, *SoftwareX*, 2015, **1–2**, 19–25, DOI: 10.1016/j.softx.2015.06.001.

43 C. Tian, K. Kasavajhala, K. A. A. Belfon, L. Raguette, H. Huang, A. N. Migues, J. Bickel, Y. Wang, J. Pincay, Q. Wu and C. Simmerling, ff19SB: Amino-Acid-Specific Protein Backbone Parameters Trained against Quantum Mechanics Energy Surfaces in Solution, *J. Chem. Theory Comput.*, 2020, **16**(1), 528–552, DOI: 10.1021/acs.jctc.9b00591.

44 J. Abramson, J. Adler, J. Dunger, R. Evans, T. Green, A. Pritzel, O. Ronneberger, L. Willmore, A. J. Ballard, J. Bambrick, S. W. Bodenstein, D. A. Evans, C.-C. Hung, M. O'Neill, D. Reiman, K. Tunyasuvunakool, Z. Wu, A. Žemgulytė, E. Arvaniti, C. Beattie, O. Bertolli, A. Bridgland, A. Cherepanov, M. Congreve, A. I. Cowen-Rivers, A. Cowie, M. Figurnov, F. B. Fuchs, H. Gladman, R. Jain, Y. A. Khan, C. M. R. Low, K. Perlin, A. Potapenko, P. Savy, S. Singh, A. Stecula, A. Thillaisundaram, C. Tong, S. Yakneen, E. D. Zhong, M. Zielinski, A. Žídek, V. Bapst, P. Kohli, M. Jaderberg, D. Hassabis and J. M. Jumper, Accurate Structure Prediction of Biomolecular Interactions with AlphaFold 3, *Nature*, 2024, **630**(8016), 493–500, DOI: 10.1038/s41586-024-07487-w.

45 E. F. Pettersen, T. D. Goddard, C. C. Huang, G. S. Couch, D. M. Greenblatt, E. C. Meng and T. E. Ferrin, UCSF Chimera—A Visualization System for Exploratory Research and Analysis, *J. Comput. Chem.*, 2004, **25**(13), 1605–1612, DOI: 10.1002/jcc.20084.

46 Z. Liu, M. A. Meyers, Z. Zhang and R. O. Ritchie, Functional Gradients and Heterogeneities in Biological Materials: Design Principles, Functions, and Bioinspired Applications, *Prog. Mater. Sci.*, 2017, **88**, 467–498, DOI: 10.1016/j.pmatsci.2017.04.013.

47 M. Levêque, Y. Xiao, L. Durand, L. Massé, E. Garanger and S. Lecommandoux, Aqueous Synthesis and Self-Assembly of Bioactive and Thermo-Responsive HA-*b*-ELP Bioconjugates, *Biomater. Sci.*, 2022, **10**(22), 6365–6376, DOI: 10.1039/D2BM01149B.

48 E. Garanger, S. R. MacEwan, O. Sandre, A. Brûlet, L. Bataille, A. Chilkoti and S. Lecommandoux, Structural Evolution of a Stimulus-Responsive Diblock Polypeptide Micelle by Temperature Tunable Compaction of Its Core, *Macromolecules*, 2015, **48**(18), 6617–6627, DOI: 10.1021/acs.macromol.5b01371.

49 B. P. Bastakoti, S. Guragain, K. Nakashima and Y. Yamauchi, Stimuli-Induced Core–Corona Inversion of Micelle of Poly(Acrylic Acid)-Block-Poly(N-Isopropylacrylamide) and Its Application in Drug Delivery, *Macromol. Chem. Phys.*, 2015, **216**(3), 287–291, DOI: 10.1002/macp.201400440.

50 H. Kang, D. J. Long and C. L. Haynes, Preparation of Colloidally Stable Positively Charged Hollow Silica Nanoparticles: Effect of Minimizing Hydrolysis on ζ Potentials, *Langmuir*, 2019, **35**(24), 7985–7994, DOI: 10.1021/acs.langmuir.9b01042.

51 Z. Tao, B. B. Toms, J. Goodisman and T. Asefa, Mesoporosity and Functional Group Dependent Endocytosis and Cytotoxicity of Silica Nanomaterials, *Chem. Res. Toxicol.*, 2009, **22**(11), 1869–1880, DOI: 10.1021/tx900276u.

52 C. A. Figg, R. N. Carmean, K. C. Bentz, S. Mukherjee, D. A. Savin and B. S. Sumerlin, Tuning Hydrophobicity To Program Block Copolymer Assemblies from the Inside Out, *Macromolecules*, 2017, **50**(3), 935–943, DOI: 10.1021/acs.macromol.6b02754.

53 J. Durairaj, A. M. Waterhouse, T. Mets, T. Brodiazhenko, M. Abdullah, G. Studer, G. Tauriello, M. Akdel, A. Andreeva, A. Bateman, T. Tenson, V. Hauryliuk, T. Schwede and J. Pereira, Uncovering New Families and Folds in the Natural Protein Universe, *Nature*, 2023, **622**(7983), 646–653, DOI: 10.1038/s41586-023-06622-3.

54 R. S. Fernandes, I. M. Raimundo and M. F. Pimentel, Revising the Synthesis of Stöber Silica Nanoparticles: A Multivariate Assessment Study on the Effects of Reaction Parameters on the Particle Size, *Colloids Surf. Physicochem. Eng. Asp.*, 2019, **577**, 1–7, DOI: 10.1016/j.colsurfa.2019.05.053.

55 G.-L. Davies, A. Barry and Y. K. Gun'ko, Preparation and Size Optimisation of Silica Nanoparticles Using Statistical Analyses, *Chem. Phys. Lett.*, 2009, **468**(4), 239–244, DOI: 10.1016/j.cplett.2008.12.031.

56 X. Li, T. Yang, Q. Gao, J. Yuan and S. Cheng, Biomimetic Synthesis of Copolymer–Silica Nanoparticles with Tunable Compositions and Surface Property, *J. Colloid Interface Sci.*, 2009, **338**(1), 99–104, DOI: 10.1016/j.jcis.2009.05.074.

57 I. A. Rahman and V. Padavettan, Synthesis of Silica Nanoparticles by Sol-Gel: Size-Dependent Properties, Surface Modification, and Applications in Silica-Polymer Nanocomposites—A Review, *J. Nanomater.*, 2012, **2012**(1), 132424, DOI: 10.1155/2012/132424.

58 T. Song, F. Gao, S. Guo, Y. Zhang, S. Li, H. You and Y. Du, A Review of the Role and Mechanism of Surfactants in the

Morphology Control of Metal Nanoparticles, *Nanoscale*, 2021, **13**(7), 3895–3910, DOI: 10.1039/D0NR07339C.

59 Y. Jang, W. T. Choi, W. T. Heller, Z. Ke, E. R. Wright and J. A. Champion, Engineering Globular Protein Vesicles through Tunable Self-Assembly of Recombinant Fusion Proteins, *Small*, 2017, **13**(36), 1700399, DOI: 10.1002/smll.201700399.

60 J. Shin and Y. Jang, Rational Design and Engineering of Polypeptide/Protein Vesicles for Advanced Biological Applications, *J. Mater. Chem. B*, 2023, **11**(37), 8834–8847, DOI: 10.1039/D3TB01103H.

61 J. Powers, J. Shin, F. Rizwan, S. H. Hong and Y. Jang, Cell-Free Protein Synthesis of Fusion-Protein Building Blocks Enables Autonomous Growth in Globular Protein Vesicle Protocells, *Biomacromolecules*, 2025, **26**(6), 3879–3887, DOI: 10.1021/acs.biomac.5c00494.

62 A. Blanazs, S. P. Armes and A. J. Ryan, Self-Assembled Block Copolymer Aggregates: From Micelles to Vesicles and Their Biological Applications, *Macromol. Rapid Commun.*, 2009, **30**(4–5), 267–277, DOI: 10.1002/marc.200800713.

63 Y. Lu, J. Lin, L. Wang, L. Zhang and C. Cai, Self-Assembly of Copolymer Micelles: Higher-Level Assembly for Constructing Hierarchical Structure, *Chem. Rev.*, 2020, **120**(9), 4111–4140, DOI: 10.1021/acs.chemrev.9b00774.

64 X. Zhou, L. Sumrow, K. Tashiro, L. Sutherland, D. Liu, T. Qin, M. Kato, G. Liszczak and S. L. McKnight, Mutations Linked to Neurological Disease Enhance Self-Association of Low-Complexity Protein Sequences, *Science*, 2022, **377**(6601), eabn5582, DOI: 10.1126/science.abn5582.

65 G. W. Buchko, S. T. Mergelsberg, B. J. Tarasevich and W. J. Shaw, Residue-Specific Insights into the Intermolecular Protein–Protein Interfaces Driving Amelogenin Self-Assembly in Solution, *Biochemistry*, 2022, **61**(24), 2909–2921, DOI: 10.1021/acs.biochem.2c00522.

66 E. C. Hartman, M. J. Lobba, A. H. Favor, S. A. Robinson, M. B. Francis and D. Tullman-Ercek, Experimental Evaluation of Coevolution in a Self-Assembling Particle, *Biochemistry*, 2019, **58**(11), 1527–1538, DOI: 10.1021/acs.biochem.8b00948.

67 P. Bauer, R. Elbaum and I. M. Weiss, Calcium and Silicon Mineralization in Land Plants: Transport, Structure and Function, *Plant Sci.*, 2011, **180**(6), 746–756, DOI: 10.1016/j.plantsci.2011.01.019.

68 E. Trembath-Reichert, J. P. Wilson, S. E. McGlynn and W. W. Fischer, Four Hundred Million Years of Silica Biomineralization in Land Plants, *Proc. Natl. Acad. Sci. U. S. A.*, 2015, **112**(17), 5449–5454, DOI: 10.1073/pnas.1500289112.

69 M. Silvander, G. Karlsson and K. Edwards, Vesicle Solubilization by Alkyl Sulfate Surfactants: A Cryo-TEM Study of the Vesicle to Micelle Transition, *J. Colloid Interface Sci.*, 1996, **179**(1), 104–113, DOI: 10.1006/jcis.1996.0192.

70 J. P. Patterson, E. G. Kelley, R. P. Murphy, A. O. Moughton, M. P. Robin, A. Lu, O. Colombani, C. Chassenieux, D. Cheung, M. O. Sullivan, T. H. I. Epps and R. K. O'Reilly, Structural Characterization of Amphiphilic Homopolymer Micelles Using Light Scattering, SANS, and Cryo-TEM, *Macromolecules*, 2013, **46**(15), 6319–6325, DOI: 10.1021/ma4007544.

71 S. A. Walker and J. A. Zasadzinski, Electrostatic Control of Spontaneous Vesicle Aggregation, *Langmuir*, 1997, **13**(19), 5076–5081, DOI: 10.1021/la970094z.

72 P. Lim Soo and A. Eisenberg, Preparation of Block Copolymer Vesicles in Solution, *J. Polym. Sci., Part B: Polym. Phys.*, 2004, **42**(6), 923–938, DOI: 10.1002/polb.10739.

73 Y. Mai and A. Eisenberg, Self-Assembly of Block Copolymers, *Chem. Soc. Rev.*, 2012, **41**(18), 5969–5985, DOI: 10.1039/C2CS35115C.

74 B. P. Allen, Z. M. Wright, H. F. Taylor, T. J. Oweida, S. Kader-Pinky, E. F. Patteson, K. M. Bucci, C. A. Cox, A. S. Senthilvel, Y. G. Yingling and A. S. Knight, Mapping the Morphological Landscape of Oligomeric Di-Block Peptide–Polymer Amphiphiles, *Angew. Chem., Int. Ed.*, 2022, **61**(14), e202115547, DOI: 10.1002/anie.202115547.

75 C. Vicente-Garcia and I. Colomer, Lipopeptides as Tools in Catalysis, Supramolecular, Materials and Medicinal Chemistry, *Nat. Rev. Chem.*, 2023, **7**(10), 710–731, DOI: 10.1038/s41570-023-00532-8..